Size Effect in Single Crystal Copper Examined with Spherical Indenters

STANISŁAW KUCHARSKI and STEFANIA WOŹNIACKA

The increasing hardness with decreasing penetration depth, referred to as indentation size effect (ISE) was previously investigated experimentally and theoretically by many researchers, however the mechanisms responsible for ISE are still being discussed. Generally, ISE is related to the density of geometrically necessary dislocation stored within a small volume beneath the indenter tip. In this study ISE is investigated experimentally in a single crystal copper using spherical indenter tips of different radii. Some new aspects of ISE are shown: a qualitative change of shape of residual impression (pile-up/sink-in pattern) when tip radius or load is modified, an increase of maximum pop-in load with decrease of tip radius as well as the well-known increase of hardness when tip radius decreases are analyzed. As we observe a difference of the residual imprint morphology which depends on tip radius and load, we apply two methods of hardness estimation: true hardness and nominal hardness. The former is determined on the basis of direct measurement of the contact area while accounting for a specific pile-up pattern, while the latter is determined by measuring the contact area using residual penetration depth. We show that hardness–tip radius relationship has a linear form for the nominal hardness and bilinear form for the true hardness.

https://doi.org/10.1007/s11661-019-05160-w

I. INTRODUCTION

THE size effect, sometimes referred to as ''smaller is stronger'', has been investigated using different experiments including micro-beam tension, micro pillar compression, and indentation. A review concerning materials mechanical size effect was presented by Zhu *et al*.[1] In the study two categories of size effect were distinguished: the intrinsic, resulting from microstructural constraints, and the extrinsic, caused by dimensional constraints (*e.g*., small sample size). The indentation size effect (ISE) was categorized as the extrinsic size effect with three-dimensional constraints. The interaction of extrinsic and intrinsic size effects was considered.

In the case of ISE, two types of experiments can be distinguished: sharp indentation (using Berkovich and Vickers tips) and spherical indentation. In a majority of papers sharp indentation was analyzed where the size effect manifested as an increase of hardness with diminishing penetration depth. This relationship was often presented as a diagram of square of hardness *vs* the inverse of penetration depth and according to earlier investigations had a linear character. This linear form was correctly captured by the first ISE model proposed by Nix and Gao[2] where ISE was attributed to the density of geometrically necessary dislocations (GND) generated beneath the indenter.

In more recent papers, where very small penetration depths were considered, results showed that the relationship between square of hardness and inverse of penetration depth deviates from linearity and should be approximated by a bilinear form.[3,4] Therefore, the Nix-Gao model was later corrected using two different approaches. In the first it was assumed that there was an upper limit of GND density (saturation of GND) that can be achieved.[5] In the second[3,6,7] it was assumed that the storage volume for GND was greater than previously estimated in the original Nix-Gao model. The approach was applied to model ISE in polycrystalline copper,[6] and nickel,[7] where both spherical and pyramidal indentation were analyzed. These corrections enabled an agreement of the Nix-Gao model with bilinear behavior of squared hardness. The newest experimental observations indicated that the density of GND is not constant; GND are not uniformly distributed, and constitute a type of sub-grain structure.[8,9]

Constitutive models of small scale plasticity were also developed, where the GND were associated with a plastic strain gradient. The well-known constitutive relations for classical plasticity were enhanced with the

STANISŁAW KUCHARSKI and STEFANIA WOŹNIACKA are with the Institute of Fundamental Technological Research, Pawińskiego 5b, 02-106, Warsaw, Poland. Contact e-mail: skuchar@ippt.pan.pl

Manuscript submitted July 10, 2018.
Article published online March 7, 2019

term that corresponded to the strain gradient. An exhaustive review of experiments and models concerning ISE were presented by Pharr *et al.*[10] In the majority of papers on ISE, the gradient enhancement of plasticity theory was applied to isotropic material models (*e.g.,* Reference 5). There are also works where strain gradient was incorporated in crystal plasticity in a manner suitable for predicting ISE (*e.g.*, Gao *et al.*,[11] Han *et al.*,[12] Petryk and Stupkiewicz[13]).

In a much smaller number of papers, the size effect was measured using spherical indentation. With spherical indentation the analysis is more complex, as the hardness depends on both penetration depth and tip radius. On the other hand, for spherical indentation the stress concentration is much lower than in the case of sharp indentation and therefore numerical simulation of the test using complex material laws is more reliable and can be performed at lower computational costs. For a fixed tip radius, R, the hardness increases when penetration depth increases, which is an effect of work hardening of the material, and is usually presented as hardness (mean contact pressure) *vs* normalized contact radius, a/R, diagram. Generally, in spherical indentation, ISE is manifested by changing the radius of the sphere. When the tip radius decreases the whole hardness-contact radius curve shifts upwards.[1,4,14–16] Swadener *et al.* investigated a variation of hardness of polycrystalline iridium in indentation tests performed with Berkovich tip and spherical tips with different radii.[4] A correlation of the indentation size effect determined with the spherical and pyramidal indenter was shown. It was observed that the predictions of the Nix-Gao model deviate from experimental results at small radii of spherical tip.

The indentation size effect in polycrystalline FCC metals (Al, Ni, Cu, Ir) was investigated with spherical indenters by Spary *et al.*[15] The authors used the Tabor relations, where the uniaxial stress equals $p_m/2.8$ (p_m—mean pressure) and the uniaxial strain equals $0.2a/R$ (a—contact radius) and they compared the data of indentation tests made with tips of different radii. It was shown that the increase of yield stress in the investigated materials was proportional to the inverse cube of the indenter radius. It was found that the numerical simulation of size effect could be performed within classical isotropic plasticity by a simple increase in the value of uniaxial yield stress without any change of the strain hardening rate.

Hou *et al.* studied the size effect and its interaction with the Hall-Petch effect in the spherical indentation of copper.[16] Tips with different radii (3.3-200 μm) were used to perform indentation tests of polycrystalline copper. The single crystal copper was indented with 3.3 and 16 μm tips. The indentation pressure-indentation strain (p_m *vs* a/R) curves were analyzed. The contact radius (used to calculate contact area and a/R) was specified from residual impression measurement. It was shown that for fixed a/R the hardness is proportional to the inverse square root of the contact radius or grain size (ISE or Hall-Petch effect). The function was found to enable prediction of the hardness of copper corresponding to $a/R = 0.25$ for any grain size and any indenter radius.

Indentation with a Berkovich tip was used to study structural and indentation size effects.[17] The analogous results observed earlier for spherical indentation[16] were also presented and a comparison of effects corresponding to both indenter types were analyzed on the basis of slip distance theory. It was concluded that structural and indentation size effects are components of the same plasticity mechanism.

In both papers[16,17] the residual impression dimensions were measured to estimate contact area and to calculate hardness. It should be noted that hardness estimation based on the measurement of residual impression was also performed elsewhere.[18,19]

The depth dependence of pile-up patterns produced with Berkovich tip in single crystal copper was investigated by Kucharski *et al.*[20] It was shown that the pile-up pattern does not change in a self-similar way when the load decreases.

In this study, the extrinsic ISE was investigated, that is we examined a single crystal copper with spherical tips having different radii. Both load-penetration curves (P-h) and topographies of residual imprints were carefully measured. The shapes of contact boundaries and pile-up/sink-in patterns were compared for different loads and different tip radii. The contact area required to specify hardness was estimated using two methods. In the first it is calculated on the basis of residual penetration depth and therefore the material anisotropy influence the contact area only through indentation direction.

In the second method the contact area was measured directly on residual impression, and therefore it is influenced by both effects of anisotropy: indentation direction and a specific pile-up/sink-in pattern. We showed that in the indentation test in anisotropic single crystal copper a specific pile-up pattern was generated that changed qualitatively when the tip radius diminished. This pile-up pattern influenced contact area and consequently hardness. The load-penetration curves and pop-in effects corresponding to different radii were shown.

II. EXPERIMENTAL

A. *Samples Preparation, Test Equipment and Test Details*

The spherical indentation tests were performed on (001)-oriented copper single crystals. High-purity (99.9999 pct) Cu single crystals, produced by the Czochralski method, were acquired from MaTecK GmbH (Germany). The crystals were cut into samples by spark erosion and a wire saw to give a (001)-oriented planar surface.

The samples were mechanically polished, then electro-polished and finally carefully cleaned with distilled water and isopropyl alcohol. The electro-polishing was used to remove a thin layer of material where the defects (that can manifest as local work hardening) were

generated during the mechanical polishing process. So, for fixed load, the penetration depth after electro-polishing increases, as the hardened layer is removed. The electro-polishing and subsequent nano-indentation test were repeated several times until the load-penetration depth curves were consistent in two subsequent steps (see Table I). On the other hand, numerous pop-in events observed in nano-indentation tests indicate that the density of defects caused by mechanical polishing or other factors was relatively low. Furthermore, a good repeatability of results shows that the influence of the polishing artifact on our results is rather negligible.

The roughness parameter Ra for the electro-polished surface was equal to approximately 1nm.

Some samples were annealed at 550 °C.

The micro- and nano-indentation tests were performed using different tip radii: $R = 1.75\ \mu$m (diamond), $R = 5.9\ \mu$m, $R = 9.2\ \mu$m, $R = 110\ \mu$m (sapphire), $R = 250\ \mu$m (tungsten carbide).

The Anton Paar MHT (micro) and UNHT (nano) testers (Open Platform equipment) were used to perform the indentation tests. The MHT micro-indenter was applied to measure load-penetration depth curves at the micro-scale. The displacement resolution and load resolution were 0.3 nm and 100 μN, respectively, and the radii of the applied tips were $R = 110\ \mu$m (sapphire) and $R = 250\ \mu$m (tungsten carbide). To scan imprints at the micro-scale, the Hommel-Etamic T8000 Nanoscan scanning profilometer, which has a vertical resolution less than 1 nm, was used. For the smallest penetration depths an optical microscope was also used to capture the residual imprints.

An ultra-nano-hardness-tester (UNHT) was used to measure load–penetration curves at the nano-scale. In the nano-system, the maximum penetration depth is $h = 50\ \mu$m and the load range is $F =$ 0-50 mN (standard range). The displacement resolution and load resolution are 0.0005 nm and 2.5 nN, respectively. The thermal drift equals 0.5 nm/min. A spherical diamond indenter tip with radius 1.75 μm and sapphire tips of 5.9 μm and 9.2 μm were used. The residual imprints generated in the nano-indentation tests were scanned using the Bruker ''Nanos'' atomic force microscope, which was integrated in the Anton Paar device.

For each indenter tip radius, six levels of load were applied. The load was selected so that the relative penetration depths h/R were close to the following values: 0.11, 0.08, 0.05, 0.02, 0.01, 0.005.

All the tests performed were load-controlled. The prescribed loading algorithm corresponds to the quasi-static regime, and the loading rate was relatively low.

Table I. Stages of Electro-polishing

Residual Penetration Depth [nm] (for $R = 1.75\ \mu$m, $P = 1.6$ mN)	Number of Electro-polishing Process
140	1
160	2
180	3
180	4

For all load levels and all tip radii the loading was performed in 120 seconds, followed by a 2 seconds pause and unloading in 60 seconds. The contact was detected with an indenter force sensor, and the applied contact force was 0.005-0.01 mN at the nano-scale and 5 mN at the micro-scale.

For each indenter tip and penetration depth the indentation test was repeated many times on different samples. This was done to verify the repeatability of the tests. We observed the pop-in effects and the scatter of results was rather low. However, for subsequent analysis only the curves that exhibited the lowest stiffness in the elastic-plastic range were selected. We believe that they corresponded to the lowest density of initially existing dislocations; that is, they were made in the regions where the initial density of dislocations was relatively low, so these regions were free of defects.

B. *Verification of Tip Radii and Frame Compliance*

The reliability of the results of spherical indentation tests strongly depends on a proper calibration of the tip geometry. The deviation of the tip geometry from the ideal spherical shape increases when the tip radius diminishes. The calibration of spherical tips using different methods including AFM measurements was discussed by Bushby *et al.*[21] As the main results presented in this paper were obtained using measurements of the topography of hardness impressions, we consistently use the topography measurements to find the actual tip radii for the applied tips. This is a simplified approach, but it is sufficiently accurate to obtain reliable results for the range of a/R ratios considered in this paper.

In the case of small tip radii (9.2, 5.9, 1.75 μm), at the nano-scale, we determined the radius of each tip in two ways. First we performed indentation tests in fused silica and compared the resulting P-h curve with the Hertz solution. On the basis of these experiments, the frame compliance was specified and the tip radius was preliminarily determined. However, in the indentation test in fused silica the maximum penetration depth is much smaller than in the case of indentation in soft copper. Therefore, to specify the tip shape for greater penetration depths, we analyzed the residual impressions in the investigated copper. The copper exhibits a low elastic modulus and very low yield strength and one can expect the elastic recovery to be relatively small, especially when the plastic deformation is large ($a/R > 0.6$), so the radius of the residual impression is very close to the radius of the tip.

The residual impressions were measured using AFM. Next, the measured area was mirrored in the Z direction; thus a spherical cavity was transformed into a sphere. The cross-section area of the sphere at various distances from the sphere top (the distance corresponds to the penetration depth in the indentation test) was specified with HommelMap software and used to generate the area function for the tip. The exemplary cross-sections of inverted impressions for $R = 5.9$ and $R = 1.75$ with the area calculated for different values of h are presented

in Figure 1. It can be seen that the shape of the cross-sections at different levels is close to circular.

In the case of our tips, the area function calculated using the above methodology can be sufficiently precisely fitted with the spherical shape and the radius specified in the indentation test in fused silica.

In Figure 2 the area function specified from the residual impression was compared with the theoretical area function corresponding to a perfect sphere, calculated as $A_p(h) = \pi*(2*h*R-h^2)$ for the range of depths applied in the tests, for $R = 1.75$ μm (a), $R = 5.9$ μm (b) and $R = 9.2$ μm (c)

In view of Figures 1 and 2, one can conclude that although the smaller tips are not perfect spheres, their area functions can be approximated with sufficient accuracy with the function corresponding to a perfect spherical shape that exhibits a constant radius. Therefore, in our approach, we consistently used the AFM measurements of residual impressions to determine the contact area, the shape of the contact perimeter and the tip radius. The latter was measured on the basis of additionally made hardness impressions, which were deeper than those used for analysis of the size effect.

The larger tips (micro-scale) were measured directly using a scanning profilometer, and a similar procedure as for small tips was applied to determine their radius and area function. As an example, the cross-sections area specified with HommelMap software at different levels for 250 and 110 μm tips are presented in Figure 3.

The area functions calculated on the basis of the profilometry measurements are compared in Figure 4 with the area functions corresponding to perfect spheres having 250 and 110 μm radii. It can be observed that both tips exhibit an almost perfect spherical shape.

In the CSM/Anton Paar experimental device there is an additional reference tip (or so-called reference fork for the micro-scale) that touches the indented surface during the indentation test and enables the indenter displacement to be measured with respect to the sample surface. Therefore, the frame compliance is very low and it can be attributed to the uncontrolled deflection of the indenter shaft rather than to the deflection of the loading frame or the deflection of the specimen mount. For each tip the frame compliance was calculated from the difference between the actual P–h curve and the Hertz solution for fused silica (see Reference 22). At the nano-scale, the frame compliance was estimated as approximately 2.1-2.3 nm/mN mN and at the micro-scale it was 0.077 nm/mN. As mentioned above, due to the specific measurement system applied in the Anton Paar device, the displacement drift is extremely low (0.0083 nm/s) and it was not corrected in our experiments.

It should be noted that the main results presented in the paper are based on the analysis of the topography of the residual impressions, which can be only slightly influenced by frame compliance and thermal drift if the tests are load-controlled.

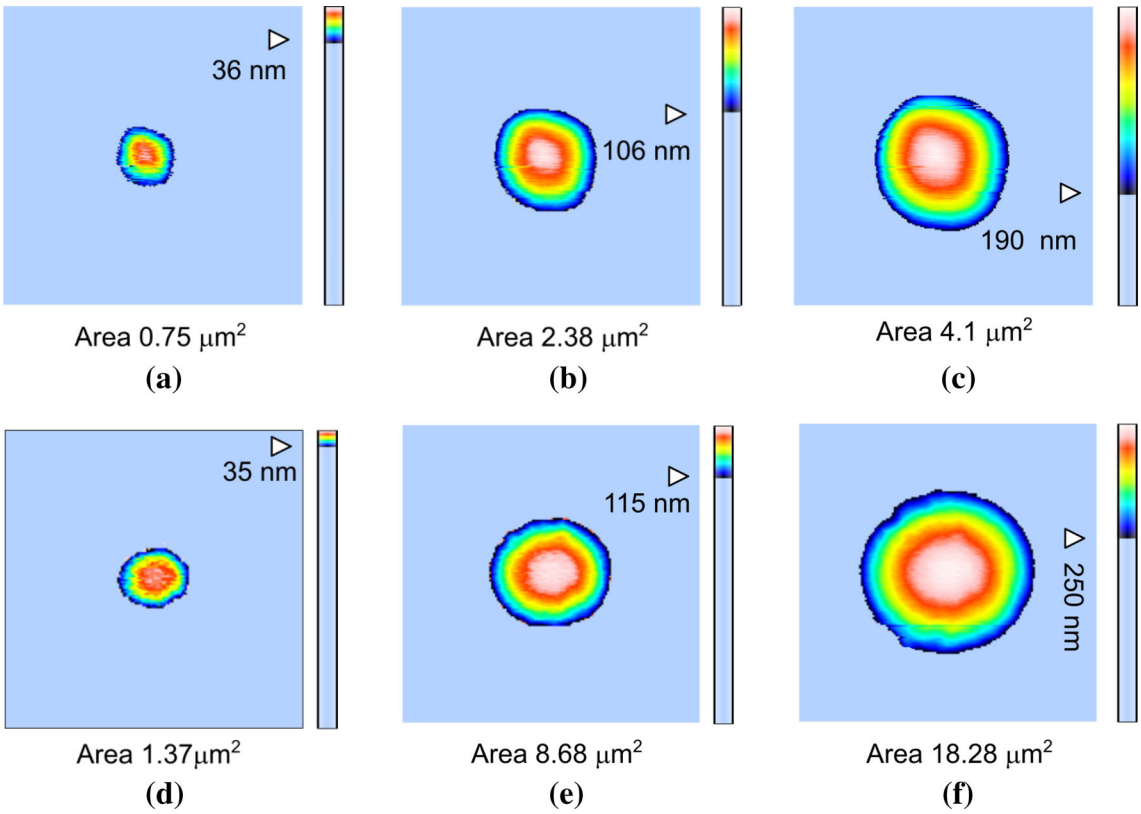

Fig. 1—Cross-sections of tips $R = 1.75$ μm (*a* to *c*) and $R = 5.9$ μm (*d* to *f*) at different levels.

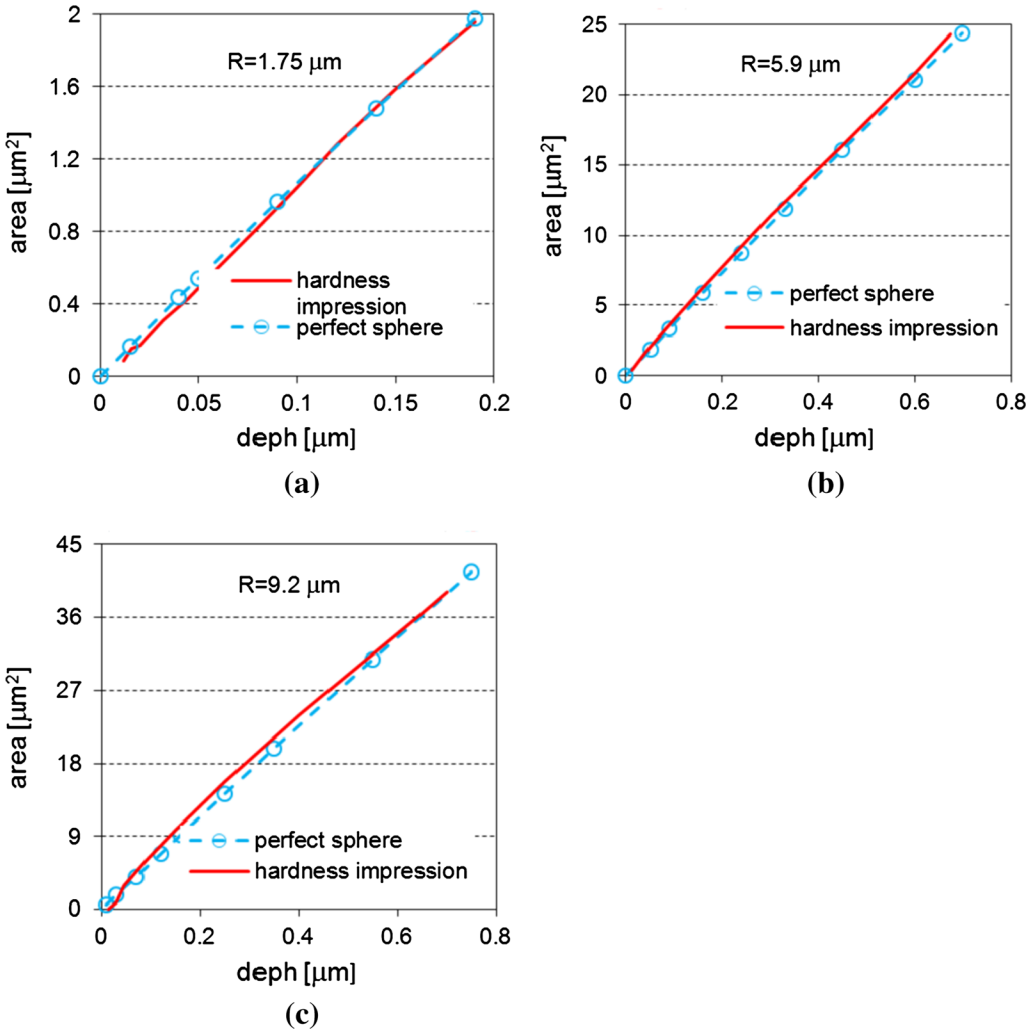

Fig. 2—Comparison of theoretical and experimental area functions for different tip radii: (*a*) $R = 1.75$ μm, (*b*) $R = 5.9$ μm, (*c*) $R = 9.2$ μm.

III. RESULTS

A. *Load-Penetration Curves*

The load-penetration curves for $R = 5.9$ μm are highlighted in Figure 5 to show the repeatability of the results. There were numerous pop-in events at different load levels, but after the pop-in event, the loading parts of the majority of curves returned to the same diagram and agreed with each other in the elastic-plastic range. The highest level of pop-in load was observed in the results for the annealed samples, where one can expect more local regions exhibiting low dislocation density than in the "as received" samples. It can also be concluded that the annealing process did not change the elastic- plastic behavior of the material after the pop-in.

The scatter of results is relatively low. However, for subsequent analysis, curves were selected that exhibited a sufficient repeatability in addition to the lowest stiffness in the elastic-plastic range.

The pop-in load has a random character and the tests with the pop-in events are characterized by an unstable load–displacement relationship. Therefore, only some of the tests presented in Figure 5 were selected for further analysis. To this end, a methodology was applied that is explained below, using as an example the tests performed with the tip $R = 5.9$ μm (Figure 5b). It should be noted that our results were based on analysis of the residual impression topography, so the unloaded state was considered and the residual penetration depth was an important parameter.

In Figure 5(b) the curves corresponding to different loads are marked with different colors, the tests that exhibit pop-in are represented with dashed lines, and those used in further analysis are marked with solid lines. In general, for the tip $R = 5.9$ μm, the following loads were applied: 0.3, 0.7, 1.75, 5, 8.5, and 13 mN. For the lowest loads, the majority of tests were entirely elastic (due to the pop-in events) and the residual impressions were not generated, or if they were, they were very shallow and the contact boundary was not sufficiently distinct. Thus, in further analysis, only the curves for 1.75, 5, 8.5, and 13 mN were taken into account, for which h/R equals 0.02, 0.05, 0.08, and 0.11, respectively. For these loads, both the purely elastic and the elastic-plastic behavior were observed. The curves corresponding to different loads are marked in different

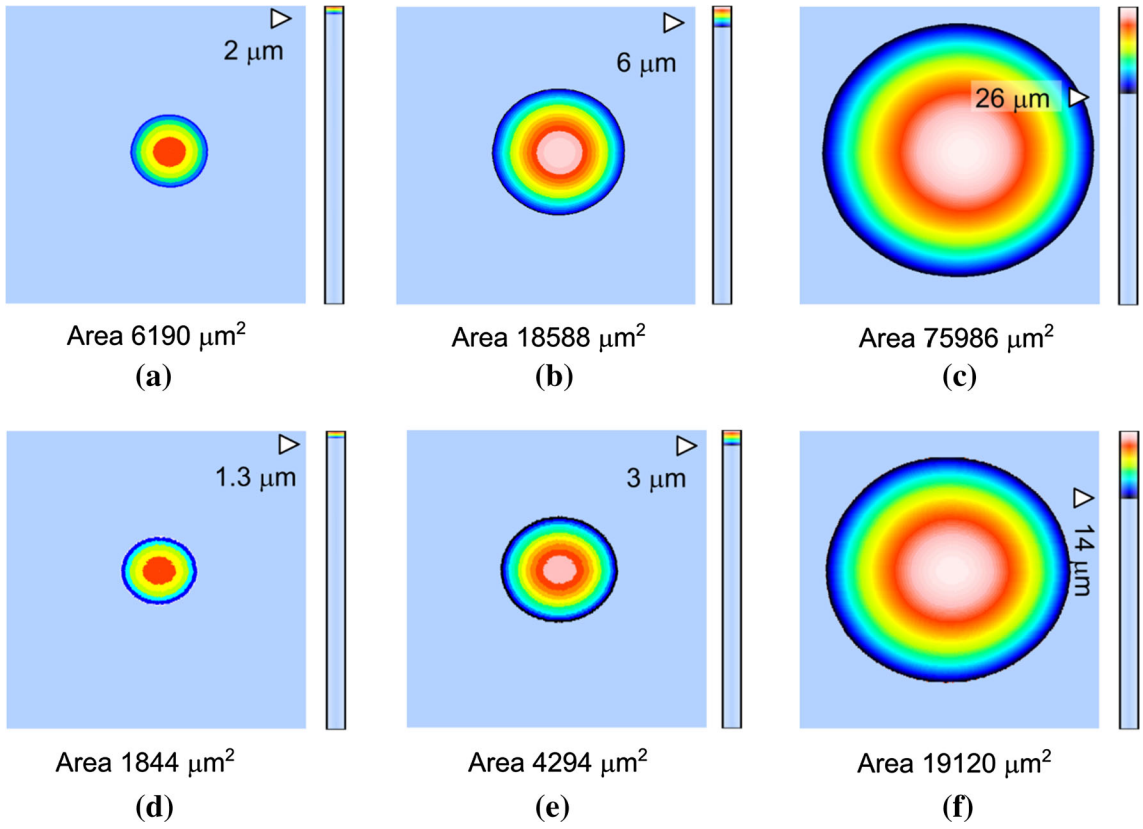

Fig. 3—Cross-sections of tips $R = 250$ μm (*a-c*) and $R = 110$ μm (*d-f*) at different levels, perfect circular shapes are evident.

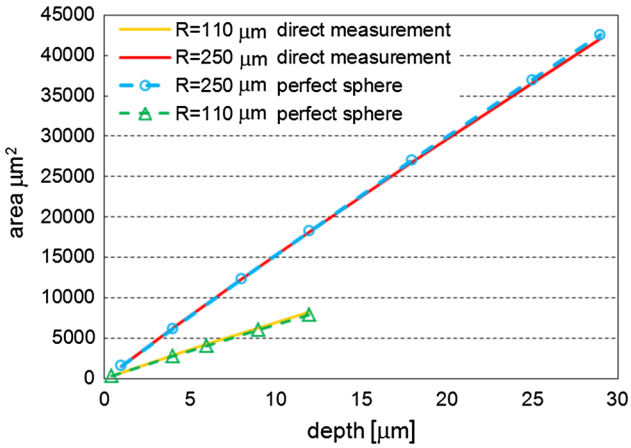

Fig. 4—Area functions for $R = 250$ μm and $R = 110$ μm tips.

colors. Many pop-in events can be seen. Prior to the pop-in, we have elastic behavior (Hertz curve), next there is strain burst where the displacement and load are not precisely defined, and after that, in the majority of cases, there follows the elastic-plastic part of the loading curve and, next, unloading. In some cases, the unloading follows immediately after the pop-in event, which is marked by the orange dashed line. It was also observed that, after the pop-in events that are generated at different loads, the same residual penetration depth can occur; *e.g.*, for the 8.5 mN load the residual penetration depth after the pop-in is the same as for 13 mN (blue dashed line and orange dashed line). The unloading can start before the pop-in and then we have a purely elastic state, *e.g.*, the orange dotted-dashed line for the 13 mN load. One observes also the unloading immediately after the pop-in, *e.g.*, the blue dashed line for the 8.5 mN load, or after elastic-plastic loading (the orange continuous line).

The elastic-plastic parts of the loading curves (solid lines or some dashed lines) that occur after pop-in events are practically the same for different loads and do not depend on the preceding instability. Therefore, the fundamental elastic-plastic P-h characteristic of the material is not affected by the pop-in events. It can be concluded that the uncertainty of the dynamic load–depth relationship associated with pop-in events does not influence our results, if only those tests are considered for which, after the pop-in event, the elastic-plastic phase of deformation occurs.

In further investigations of contact pressure or pile-up patterns, the data corresponding to *P-h* curves representative of each load level were used.

To observe the size effect in the spherical indentation, we started from the comparison of the *P-h* curves for different tip radii in the scaled $h/R - P/R^2$ reference system (Figure 6). In the diagrams two stages can be distinguished: initial elastic stage (prior to pop-in) and subsequent elastic-plastic stage. In the normalized reference system, the load-penetration curves are practically the same in the elastic range; however, after the pop-in events the curves corresponding to lower tip radii

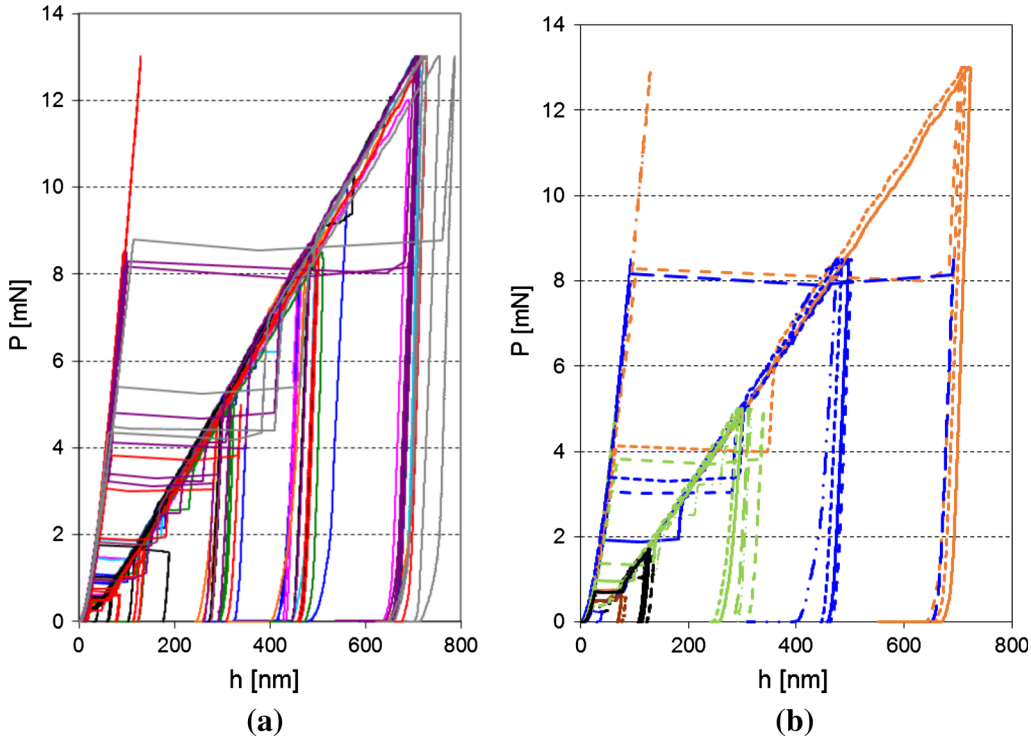

Fig. 5—Selection of representative *P-h* curves for $R = 5.9\ \mu$m: (*a*) all measurements, (*b*) curves selected for further analysis.

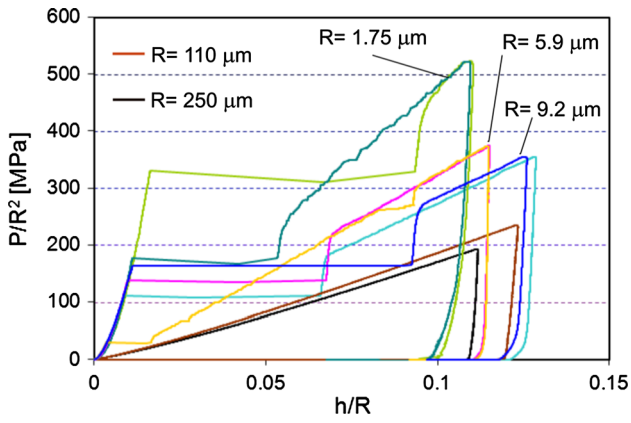

Fig. 6—Comparison of scaled *P-h* curves for different indenter radii. For the indentation at the nano-scale ($R = 9.2, 5.9, 1.75\ \mu$m) more than one curve is presented for each tip to show different levels of pop-in load and the return of *P-h* diagrams to the same elastic-plastic loading path after the pop-in. At the micro-scale the pop-in was not observed.

are stiffer. The coincidence of the load-penetration diagrams in the elastic range signifies that the radius and frame compliance corresponding to different tips were determined properly.

The diagrams made for the micro-scale were close to each other ($R = 110\ \mu$m, $R = 250\ \mu$m), the curve for $R = 9.2\ \mu$m was much stiffer than those corresponding to the micro-scale, and the stiffest behavior was observed for the indentation with a 1.75 μm radius. The difference between the curves corresponding to $R = 250\ \mu$m and $R = 9.2\ \mu$m was similar to the difference between $R = 9.2\ \mu$m and $R = 1.75\ \mu$m.

In our experiments, *e.g.*, Figures 5, 6, the pop-in events were observed. For FCC single crystal (nickel), Shim *et al.*,[23] presented a dependence of the pop-in shear stress on spherical tip radius. Lawrance *et al.*,[24] studied an effect of tip radius and grain orientation on the pop-in events in polycrystalline nickel, and a stochastic model of pop-in was presented by Phani *et al.*[25] The combined indentation and AFM investigation of pop-in events in indentation of W and Al with 1 μm spherical tip was shown by Pathak.[26] In the paper the load-displacement curve, indentation stress-indentation strain curve and an evolution of anisotropy of the residual imprint with load were analyzed. It was concluded that after a further loading, beyond pop-in event, the response of the material is essentially the same as that of a test without the pop-in event. Such a behavior was also observed in our experiments.

In general, in the papers[23–26] the pop-in was attributed to the lack of dislocations sources in a volume affected by contact stress in the initial stage of indentation with small spherical tip and subsequent immediate activation of pre-existing dislocations or nucleation of dislocation in dislocation-free zones when the load and stressed volume increase. In the latter case, the pop-in load corresponds to the theoretical strength of the material,[23] that is difficult to observe in the macro-scale. The detailed analysis and modeling of the pop-in is out of the scope of this paper. However, the presence of numerous pop-in events at different levels of load confirms an appropriate electro-polishing of the samples and a repeatability of *P-h* curves (including

residual penetration depths) in the load ranges that exceed the pop-in loads.

B. *Observation of Residual Imprints*

In the indentation tests, two forms of results can be analyzed: load-penetration curves and deformation of the indented material surface, *i.e.*, the topography of the residual imprints.

In general, the analysis of residual imprints is used in the primary definition of hardness, *i.e.*, hardness is calculated as a ratio of the applied force and projected contact area measured on the residual impression in an unloaded state. In the case of spherical indentation, it is accepted that the thus defined hardness is equivalent to the mean contact pressure (in the loaded configuration), *i.e.*, the Meyer hardness. One assumes that the change of contact area in the unloading process can be neglected, *i.e.*, the radius of the contact perimeter is practically constant, and predominantly the penetration depth diminishes. This assumption has been confirmed in many papers, *e.g.*, by Field and Swain[27] and Biwa and Storakers.[28]

The topography of the hardness impression delivers important information as, when the indentation test is performed in only one direction, the anisotropy of the material can be detected only from an analysis of the topography of the residual imprint. Our measurements indicated that there was an effect of material anisotropy on the residual impression and contact area. This effect depends on the tip radius and on the applied load.

As an example the imprint for $R = 110$ mm and $h/R = 0.11$ is shown in Figure 7. It was captured using a scanning profilometer. In Figure 7(a), a general view of the imprint is shown, and in Figure 7(b) a threshold map is visible where the pile-up pattern (four hillocks) is more evident. At the micro-scale, for tip radii of 110 and 250 μm, the shapes of the imprints were qualitatively similar.

On the other hand, in many methods applied to measure hardness, the anisotropic character of the residual imprint is neglected, as the contact area used to calculate hardness is commonly estimated on the basis of the penetration depth and the slope of the unloading curve measured in the indentation test.

In our investigations, the contact area of the tip and the indented material was estimated directly from the measured dimensions of the residual impression. Therefore an important factor was the precise detection of the contact boundary. To this end, we applied various approaches. At the micro-scale, for shallow indentations, the contact boundary was sufficiently distinct under the optical microscope (Figure 8). For greater penetration depths (h/R close to 0.1) the depth of focus in the microscope was not sufficient and 3D profilometry measurement of the residual impressions was performed. Similarly, in the nano-scale, all the residual impressions were measured using AFM. Once the indented surface topography was acquired, the Hommelmap® software, which enables contact boundary detection, was used. Two methods were applied: the edge detection procedure, and the photo simulation option that gives a photo-like image of the measured area with the distinct shape of the contact boundary. The former makes use of a gradient filter where for each measured point the most important slope in four directions is found. The area inside the contact boundary was measured using AutoCad-like software.

The shapes of the residual imprints for $R = 110$ μm and all the applied loads acquired using the scanning profilometer ($h/R = 0.11$) and optical microscope are shown in Figure 8.

The anisotropy of the single crystal was manifested and, in spite of the spherical indenter, the contact boundary had the shape of a rounded square for all the applied loads. For large loads, at the macro-scale, a similar shape was observed elsewhere.[29] Only in the case of the lowest load ($h/R = 0.005$), it is more rounded and closer to the circular shape. In general, one can conclude that when the load increased, the shape of the contact boundary became closer to the rounded square in which the rounded corners became sharper. This experimental result does not seem to be commonly known.

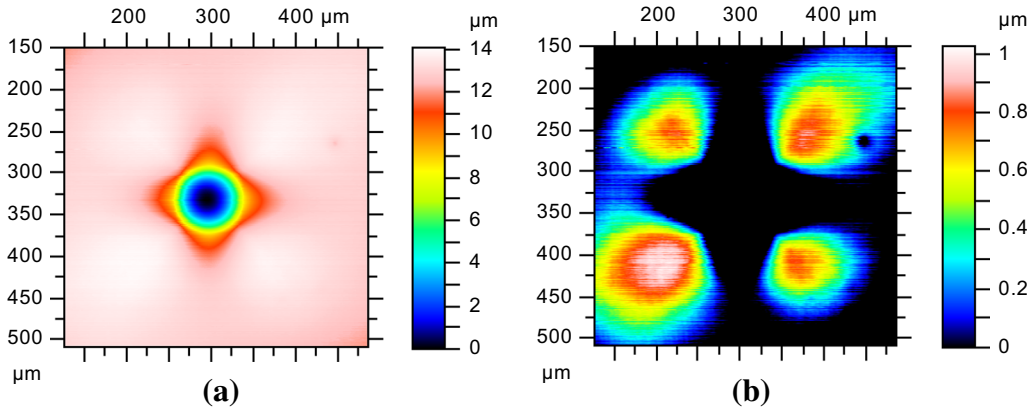

Fig. 7—Residual impression at the micro-scale measured using scanning profilometer for $h/R = 0.11$ and $R = 110$ μm: (*a*) full sale map, (*b*) threshold map—upper part of measured area.

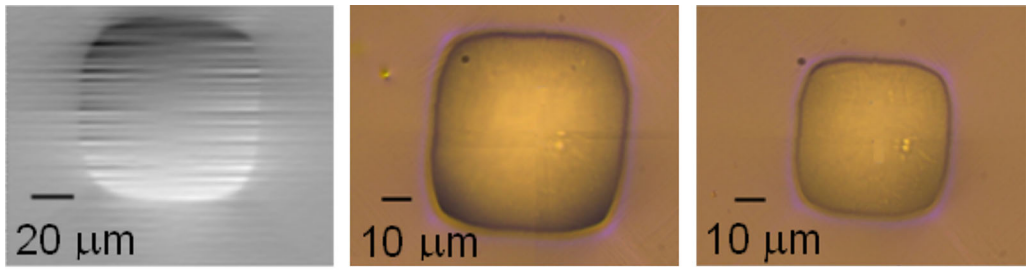

(a) h/R=0.11 **(b)** h/R=0.08 **(c)** h/R=0.05

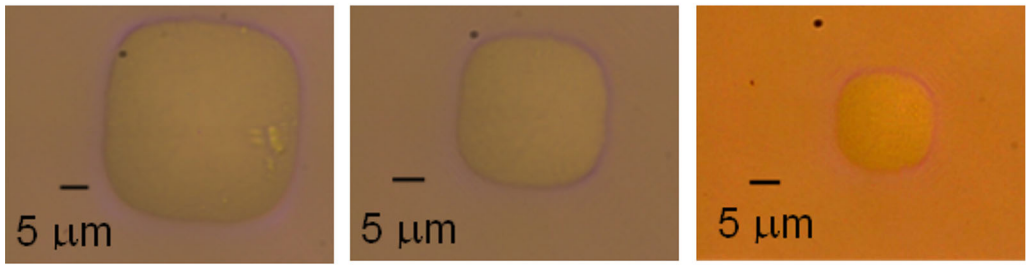

(d) h/R=0.02 **(e)** h/R=0.01 **(f)** h/R=0.005

Fig. 8—Residual impressions for $R = 110$ μm (micro-scale) for different penetration depths measured with scanning profilometer and highlighted using photo simulation procedure (*a*) and captured using optical microscope (*b* to *f*). Residual impressions for $R = 250$ μm are qualitatively similar, see Figs. 11(a) or 13.

The exemplary maps of residual imprints at the nano-scale for $R = 1.75$ μm, $R = 5.9$ μm and $R = 9.2$ μm are shown in Figure 9. The pile-up patterns are less distinct and the residual imprints are more rounded than at the micro-scale.

In Figure 10 the residual imprints made at the nano-scale with indenter tips $R = 1.75$ μm, $R = 5.9$ μm, and $R = 9.2$ μm, for the maximum ($h/R = 0.11$) and medium ($h/R = 0.05$) load are presented in the form that enables to detect contact boundary. The imprints were measured using AFM and the acquired maps were analyzed using Hommel Map® software. Two approaches were used to detect the contact boundaries of the imprints: for $R = 1.75$ μm and $R = 9.2$ μm the photo simulation option was activated, and in the case of $R = 5.9$ μm the edge detection procedure (gradient filter) was applied. After analysis of the maps of many imprints, we concluded that both the photo simulation and edge detection procedures enabled us to detect the contact boundary with similar accuracy. However, for small radii and small loads when the contact boundary is less distinct, it can be more easily recognized when the gradient filter is applied.

One can see that there is quite a different relationship between the shape of the residual imprint and the applied load compared with the micro-scale. Only one residual impression that corresponded to the greatest load and largest tip radius (9.2 μm) can be recognized as slightly similar to the rounded square. Generally, at the nano-scale, for lower loads of the $R = 9.2$ μm tip, and for other tip radii, the contact boundary had a more or less circular shape. Some observed deviation from the circular shape resulted from an insufficient accuracy of the tip manufacturing.

The results presented in Figures 9 and 10 are summarized in the diagram of the ratio of the maximum and minimum d_{max}/d_{min}, dimensions of the residual impression (Figure 11). At the micro-scale, d_{max}/d_{min}, is nearly constant and greater than 1, while at the nano-scale it is close to 1.

IV. DISCUSSION

A. *Pile-Up Patterns and Contact Area*

The size effect on variation of the sink-in/pile-up patterns can be shown in a more detailed analysis of the residual impressions. The schematic of the residual impression in the loaded and unloaded state, for isotropic materials that exhibit sink-in patterns, is presented in Figure 12. The quantities used in the analysis of the indentation tests are marked: h_p denotes the residual penetration depth, h_e is the elastic part of the total penetration depth, h_c is the contact depth, R_i is the indenter radius and R_r is the radius of the residual impression (in the unloaded state), a is the actual radius of the contact boundary. It should be noted that for the materials that exhibit a small yield stress to elastic modulus ratio, like single crystal copper, one can assume that $R_r \approx R_i = R$ without loss of accuracy. The nominal contact radius a_{nom} is calculated on the basis of the residual penetration depth using the formula $a_{nom} = \sqrt{2hR_r - h_p^2}$ and it corresponds to contact with a fictitious material that exhibits neither pile-up nor sink-in. In the case of isotropic materials, there is a parameter c^2 (Eq. [1]) that is a measure of the pile-up or

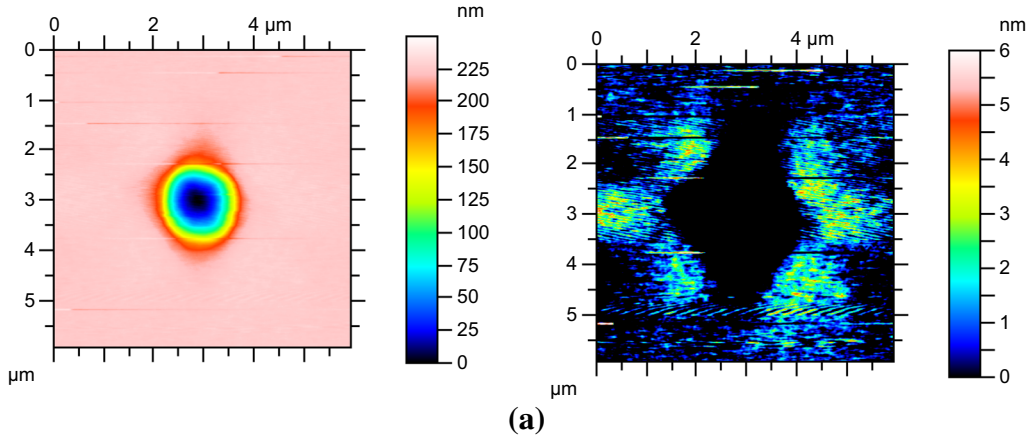

(a)

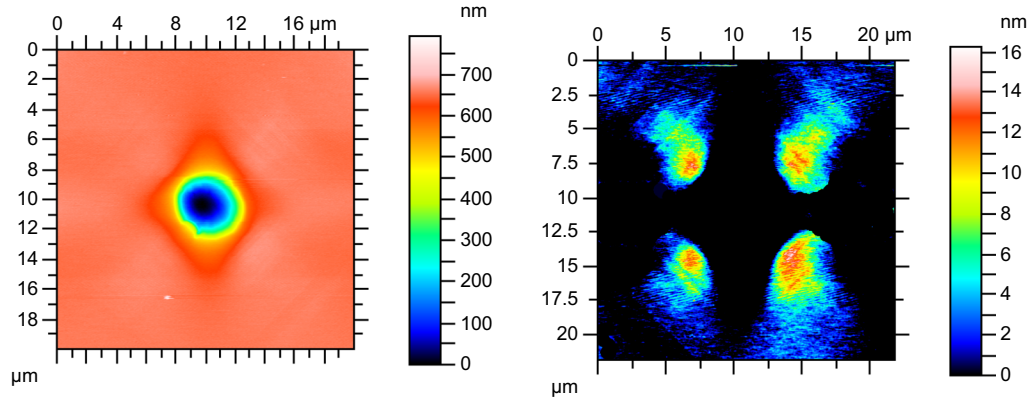

(b)

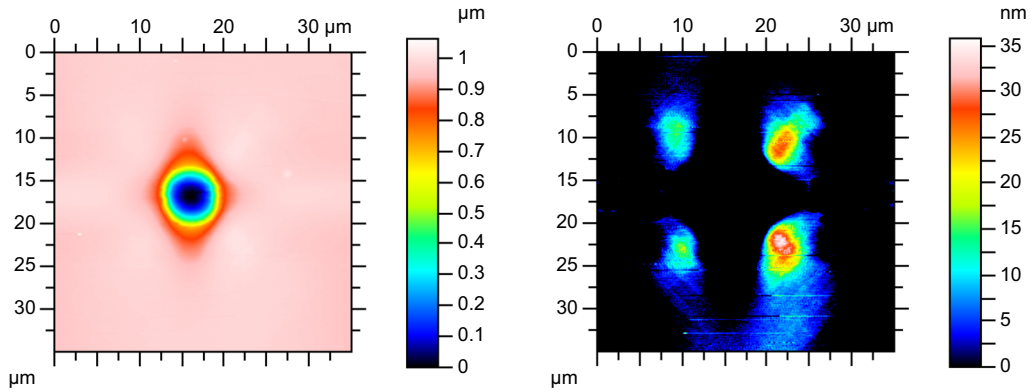

(c)

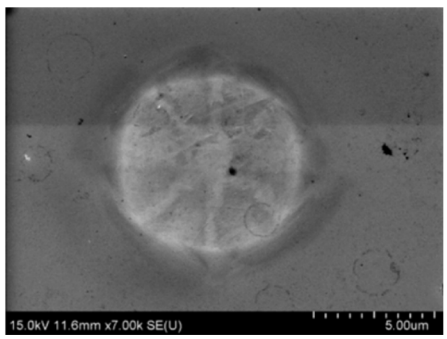

(d)

Fig. 9—Residual impressions at the nano-scale, $h/R = 0.11$. Full scale map and threshold map—upper part of measured area for (*a*) $R = 1.75$ μm, (*b*) $R = 5.9$ μm, (*c*) $R = 9.2$ μm, (*d*) $R = 9.2$ μm surface morphology acquired using SEM.

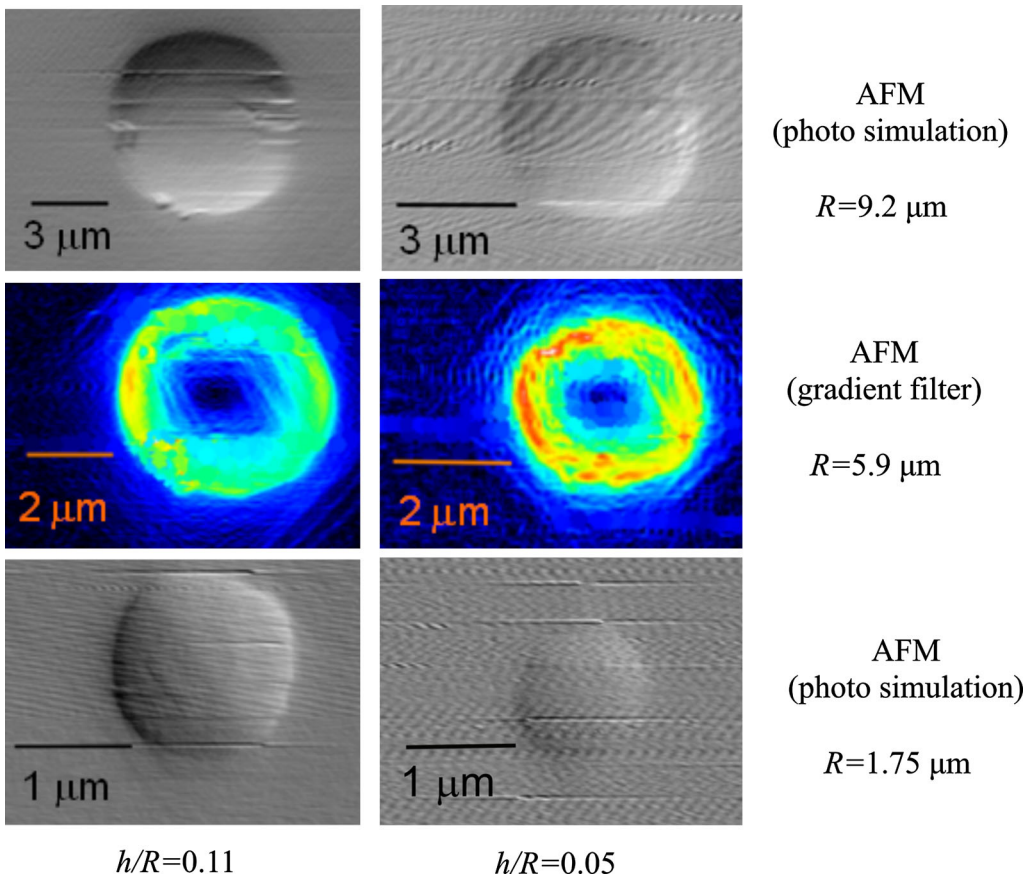

Fig. 10—Detection of shape of contact boundary for residual imprints acquired with AFM, for different tip radii and h/R ratios. Similar sharpness of contact boundaries is observed for different methods of detection of contact boundaries.

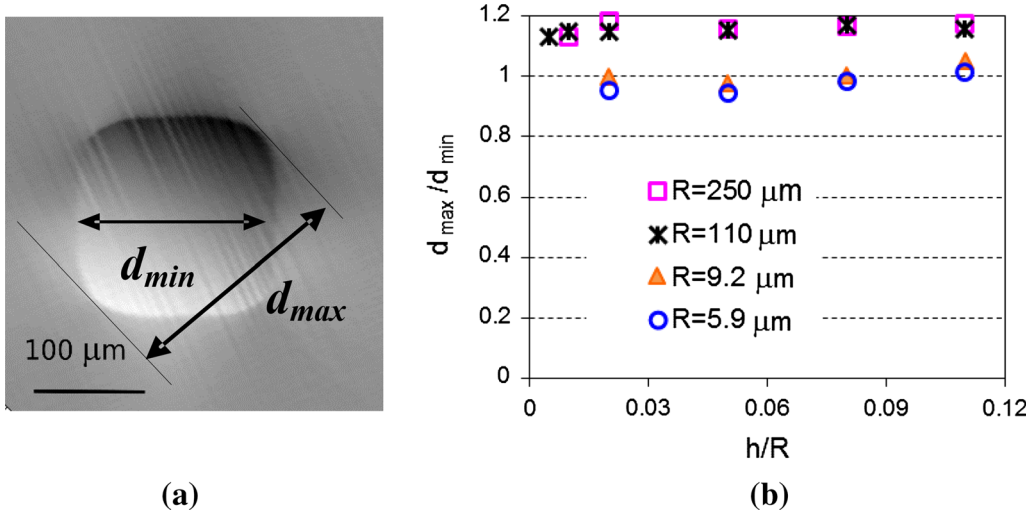

Fig. 11—Variation of shape of contact boundary: (*a*) residual impression for $R = 250$ μm, (*b*) ratio of maximum and minimum impression diameter for different penetration depths.

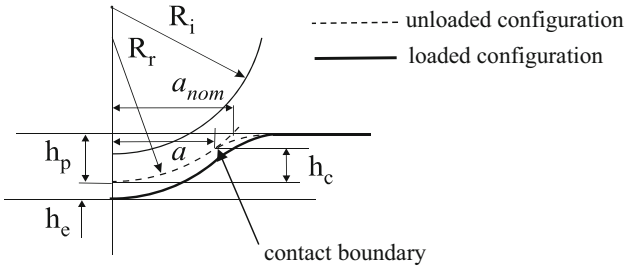

Fig. 12—Schematic of sample and indenter surface in loaded and unloaded state for isotropic material that exhibit sink-in pattern.

sink-in in the indentation test. It was originally defined for small penetration depths ($a/R < 0.22$)[30] as a function of residual penetration depth h_p and contact radius a (Figure 12).

$$c^2 = \frac{a^2}{2h_p R}. \quad [1]$$

For larger penetration depths, it can be rewritten as:

$$c^2 = \frac{a^2}{2h_p R - h_p^2}. \quad [2]$$

When the indented material exhibits pile-up $c^2 > 1$, in the case of sink-in $c^2 < 1$ and when $c^2 = 1$, there is neither pile-up nor sink-in and the nominal contact area is equal to the true contact area. It should be noted that, according to Eqs. [1] and [2], c^2 is equal to the ratio of the true (A) and the nominal contact area (A_{nom}) of the indenter.

$$c^2 = \frac{a^2}{2h_p R - h_p^2} = \frac{a^2}{a_{\text{nom}}^2} = \frac{A}{A_{\text{nom}}} \quad [3]$$

In the case of anisotropic single crystals considered in this paper, the above approach should be modified. The residual impression and contact area are influenced not only by the pile-up or sink-in pattern but also by the anisotropy of the material. The definition of the contact radius is not so evident due to the quasi-rectangular shape of the contact boundary, so c^2 should be calculated as the ratio of the true and nominal contact area, as seen in Eq. [3]. The true contact area A was directly measured on the basis of the contact boundary detected on the 3D map. The corresponding mean contact radius was specified as $a = \sqrt{A/\pi}$.

The nominal contact area (A_{nom}) in turn was calculated using the residual penetration depth, with the same formula as for the isotropic material, $A_{nom} = \pi a_{nom}^2 = \pi(2Rh_p - h_p^2)$. However, this definition makes it independent of the anisotropic character of the pile-up/sink-in pattern.

It should be noted that in the case of isotropic rigid-plastic materials,[30] which exhibit power law hardening, c^2 is an invariant of the spherical

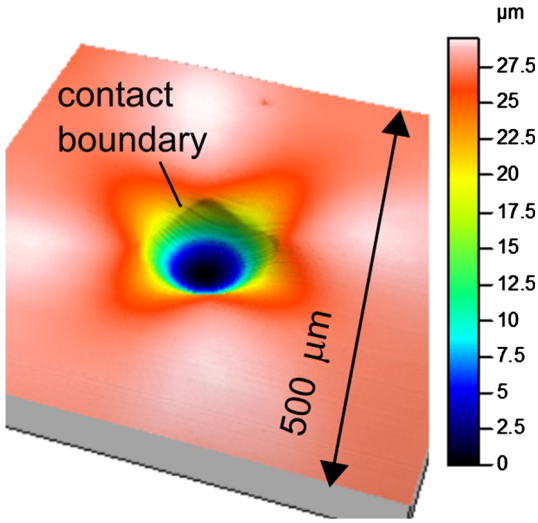

Fig. 13—3D view of residual impression for $R = 250$ μm and $h/R = 0.1$, with marked contact boundary. It exhibits a rounded square shape when projected on XY plane but its Z-coordinate is not constant. Entire contact boundary lies below the non-deformed surface.

indentation. c^2 is also constant for elastic-plastic materials for sufficiently large penetration depths and a low ratio of yield strength and elastic modulus. The latter condition is approximately fulfilled in the single crystal copper where the yield strength is low (approximately 10 MPa).[31]

For single crystal copper, we observe that the true contact area, which is measured directly, is generally lower than the nominal contact area, thus $c^2 < 1$. However, the exact value of c^2 depends on the indenter radius. At the micro-scale ($R = 110$ μm, 250 μm), the corresponding value of c^2 is 0.75. Thus, in spite of the observed four hillocks around the residual imprint in Figure 7, the contact perimeter is located below the level of the non-deformed surface (Figure 13), and we effectively have the sink-in pattern, *i.e.*, the true contact area is much smaller than the nominal contact area.

The influence of friction on c^2 was analyzed by Mesarovic and Fleck[32] for isotropic materials. They stated that, in the limiting case, *i.e.*, sticking friction, the change of c^2 is about 8 pct with respect to the frictionless state. In our work, c^2 at the micro-scale was estimated as equal to 0.75, so it is distinctly smaller than 1 and we have a sink-in pattern. In view of the relatively small influence of friction, one can conclude that the sink-in pattern is an effect of material properties rather than an effect of friction.

Figure 14 shows the normalized profiles of the residual imprints for different tip radii and the largest penetration depth $h/R = 0.11$. It can be seen that for fixed h/R, when the tip radius decreases, the sink-in pattern is less evident, the contact boundary is shifted upwards, and the true contact area becomes closer to the nominal contact area (*i.e.*, c^2 increases and becomes closer to 1). It should be noted that the value of c^2 does not reach 1, even for the smallest tip radius.

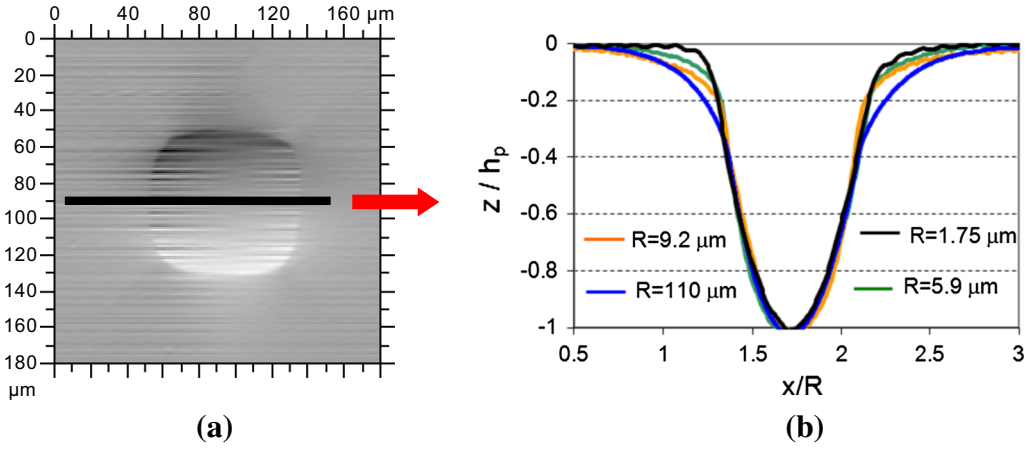

Fig. 14—Profiles across the residual impression in scaled reference system: (*a*) profile direction, (*b*) changes of sink-in pattern with tip radius for $h/R = 0.11$.

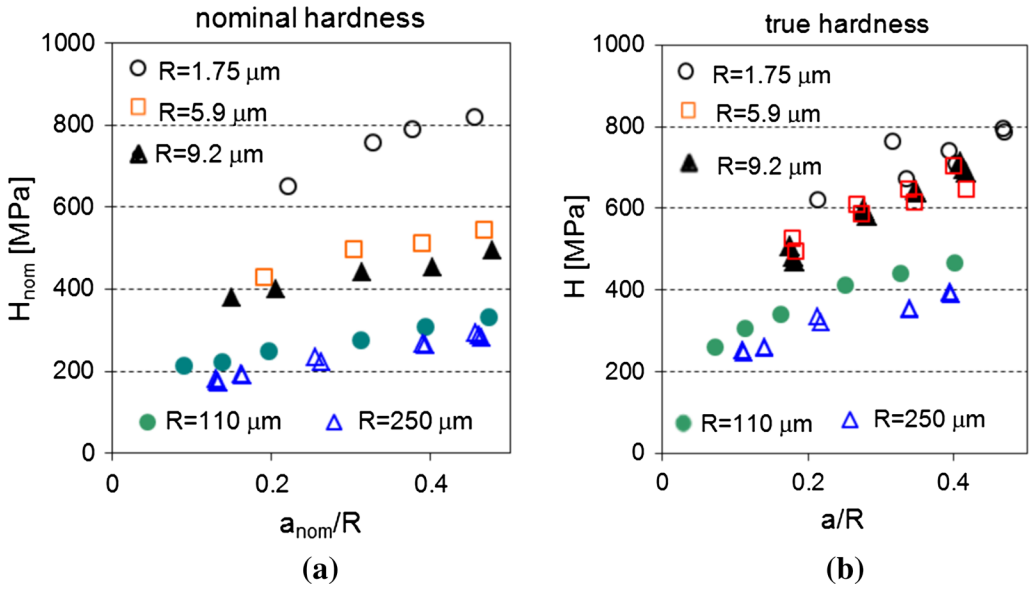

Fig. 15—Hardness *vs* indentation strain, a/R, for different tip radii: (*a*) nominal hardness, (*b*) true hardness.

B. *Estimation of Hardness*

The observed sink-in pattern is a measure of the difference between the nominal and true contact area, which in turn yields the difference between the true hardness ($H_{tr} = P/A$) and nominal hardness ($H_{\text{nom}} = P/A_{\text{nom}}$). The hardness values specified using two different methods as a function of the contact radius and tip radius ratio are shown in Figure 15.

Qualitatively, both methods of hardness measurement (nominal hardness and true hardness) lead to similar results, *i.e.*, the increase of hardness when the tip radius decreases. In both methods, the hardness increases with load and the hardness curves shift upwards for decreasing tip radii. However, in the case of nominal hardness, this shift is different from that observed for true hardness. For nominal hardness we have distinctly separate curves that correspond to the different tip radii, and the difference between these curves is relatively large, so they can be easily distinguished. The highest hardness corresponds to a 1.75 μm tip radius and it is much greater than that measured for other tips in the nano-scale.

In the case of true hardness, the effect of the tip radius has a different character. The true hardness, due to the sink-in effect, is generally greater than the nominal hardness (see Figure 15(b)). At the micro-scale (110 and 250 μm tips), the difference between the true hardness values corresponding to different radii is evident, but it decreases at the nano-scale where the true hardness curves for $R = 5.9$ and $R = 9.2$ μm are similar. The greatest values of the true hardness are observed for $R = 1.75$ μm, although at some points it is relatively close to the values measured for the 5.9 and 9.2 μm tip radii. It should be noted that there is a large difference between the values measured at micro- and nano-scale

For all the applied tip radii (except 1.75 μm), the true hardness is greater than the nominal hardness and this is an effect of sink-in. For $R = 1.75$ μm the true hardness at some points is lower than the nominal hardness. This may be the result of an inaccurate measurement of the contact area or an effect of the generation of pile-up instead of a sink-in pattern when the smallest tip is used. However, it can be seen that the true and nominal hardness values corresponding to $R = 1.75$ μm are similar.

The difference between the hardness corresponding to the smallest and greatest tip radius is observed in both the nominal and true hardness diagrams; however, in the latter case the difference is smaller.

The diagrams of hardness *vs* a/R (Figure 15) can be compared with those reported by Hou *et al.* for single crystal.[16] They have shown that the relationship H-a/R is similar to that presented in Figure 15. It should be noted that in the paper by Hou,[16] as well as in this paper, the true hardness was reported, as the contact area was estimated from measurement of the residual impression, but only one tip radius ($R = 16$ μm), was used for single crystal copper. As can be expected, the hardness curve corresponding to this radius value[16] lay between those plotted in Figure 15(b) for $R = 110$ μm and $R = 9.2$ μm. However, in the present paper a greater strain hardening effect is observed.

The hardness for different tip radii can also be compared when the normalized contact radius a/R is fixed. According to the well-known Nix–Gao model, for spherical indentation, the hardness–tip radius relationship is similar to the hardness–penetration depth for sharp indentations.

$$\frac{H}{H_0} = \sqrt{1 + \frac{R*}{R}} \qquad [4]$$

where $R* = \overline{r}b\rho_s$, $\overline{r}$—Nye factor, b—Burgers vector, ρ_s—statistically stored dislocation density

In Figure 16, the squares of true hardness and nominal hardness are plotted against the inverse of the tip radius for $a/R = 0.25$. As can be seen in the case of nominal hardness, this relationship is linear for single crystal copper. The true hardness curve deviates from linearity and it can be fitted with two straight lines. The bilinear relation $H^2 \sim \frac{1}{R}$ for spherical indentation of single crystal copper indented with spherical tips has not been reported previously in the literature. It is a manifestation of the specific evolution of the residual impression in an anisotropic material generated in contact with an axis-symmetric spherical indenter. As shown above, when the tip radius diminishes, the contact boundary does not change in self-similar mode, but it is shifted up (Figure 14). This effect leads to a relative increase of the contact area. Therefore, the increase of true hardness with decrease of the tip radius is not as evident as the increase of nominal hardness, and the bilinear relation shown in Figure 16 should be used. The bilinear form of the square of the hardness curve measured with sharp indenters has already been reported by Feng and Nix[3] and Swadener *et al.*,[4] where it was a basis for modification of the Nix–Gao model and it was attributed to saturation of the density of GND or a greater GND storage volume than that assumed in the original Nix–Gao model.[3,5–7] A similar explanation can be applied in the case of spherical indentation, as there is no important increase of hardness when R diminishes from 9.2 to 1.75 μm.

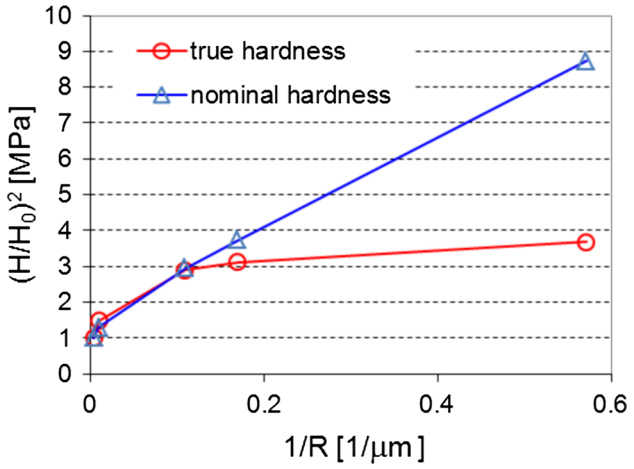

Fig. 16—Square of hardness *vs* inverse of tip radius for fixed ratio $a/R = 0.25$.

It should be noted that the anisotropy of a material manifests in different ways at the micro- and nano-scale. At the micro-scale where there is low GND density, we have both effects: a quasi- rectangular shape of the contact boundary and four hillocks that are close to this boundary (Figure 7). At the nano-scale (high GND density), the effect of anisotropy is less evident; the contact boundary has a circular shape so it is not influenced by an anisotropic deformation (Figure 10), the four hillocks are still visible, but they are less distinct, and are located at a certain distance from the contact boundary (Figure 9), where the dislocation density is lower.

The true hardness is more realistic than the nominal hardness as the latter refers to a certain fictitious area of contact that for large tip radii can be 25 pct greater than the real contact area (see Figures 14 and 15). Therefore the dislocation density used in the Taylor equation should be correlated with the true hardness rather than with the nominal hardness. For the smallest radii, the contact areas and consequently the dislocation densities are high and similar in both cases.

On the basis of the above observations, more general conclusions can be formulated. For large tip radii, when the dislocation density is low, the anisotropic character of deformation is manifested as a pile-up composed of four hillocks and a quasi-rectangular contact boundary that are an effect of glide on certain slip systems according to the crystal plasticity solution reported in many papers. In the case of a small tip radius (at the nano-scale), where there is a high dislocation density, the deformation exhibits an isotropic character (circular contact boundary) in a region very close to the contact area. However, at a certain distance from the contact

boundary, where lower dislocation density occurs, the anisotropy is still manifested and four hillocks are present similarly to the micro-scale (Figure 9). A possible explanation of this effect is that, in the high dislocation density regions, different slip systems are activated from those activated in regions of low dislocation density, *i.e.*, close to large indents (at the micro-scale) or sufficiently far from small indents (at the nano-scale). The difference in the activated slip system in different scales can result from modification of the hardening on slip systems or from a change of latent hardening (dislocation generated on different sliding planes block each other), which can be functions of the dislocation density.

The experimental results presented here can be useful in verifying the assumptions of the strain gradient models of crystal plasticity. As an example, we take the 'minimal' gradient enhancement recently proposed by Petryk and Stupkiewicz,[13] in which the internal length scale is defined by the current flow stress and thus cannot be adjusted to fit the experimental data. Their model was implemented in a finite element code and applied to three-dimensional simulations of spherical indentation in single crystal copper.[33] The numerical prediction of the dependence of the nominal hardness on the maximum penetration depth h at fixed ratio $h/R = 0.11$[33] is compared to the present experimental results in Figure 17. The agreement is excellent. This can be treated as confirmation that the internal length scale, derived from the empirical laws of crystal plasticity[13] and shown to possess a direct physical interpretation, can perhaps play a crucial role in describing the size effects observable at a micron scale in ductile metal crystals. The agreement is less clear for the actual hardness influenced by the current contact area estimates; therefore, it is not discussed here. It must be noted that in the numerical simulations the true contact area is measured under maximum load, which contrasts sharply with the contact area estimates presented in this paper. On the other hand, the experimentally observed tendency towards the circular shape of the contact boundary with a decreasing tip radius is in qualitative agreement with the simulations results.[33]

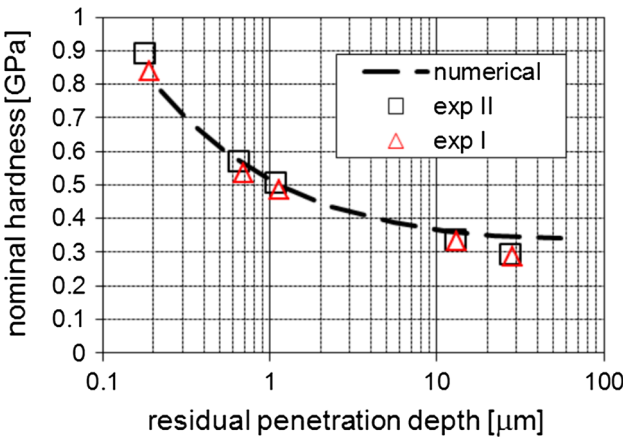

Fig. 17—Dependence of nominal hardness on the penetration depth h at fixed ratio $h/R = 0.11$, comparison with numerical results.[33]

In our paper a comparison of two approaches, *i.e.*, true hardness and nominal hardness, was proposed. Both approaches have advantages and shortcomings and have been applied in the literature (*e.g.,* [6]-nominal and [16]-true hardness). In the case of nominal hardness, some information about the material response is lost (*e.g.*, on the basis of indentation in only one direction, anisotropy of the material cannot be captured), but there is no uncertainty in the specification of the contact area as it is calculated using the penetration depth, which is precisely and directly measured in the indentation test. True hardness in turn provides more information about the material deformation mode, in particular taking into account the specific pile-up pattern generated in the material due to its anisotropy. However, there are errors resulting from a non-precise recognition of the contact boundary that can lead to erroneous estimation of the contact area. It should be noted that both approaches are used in the analysis of spherical indentation tests.

V. CONCLUSIONS

Some aspects of the size effect in spherical indentation tests of single crystal copper have been observed. The size effect manifests in the following forms: increase of hardness, modification of the shape of the contact boundary, modification of the amount of pile-up/sink-in, and increase of the normalized pop-in load with decreasing tip radius.

The well-known effect of increase of the hardness with decrease of the tip radius at fixed h/R was analyzed in more detail. It has been shown that this effect is quantitatively different, *i.e.*, more evident in the case of nominal hardness than in the case of true hardness (Figures 16 and 17). This difference results from the different deformation modes of single crystal at the micro- and nano-scale. At the micro-scale one observes a distinct sink-in pattern, so the contact boundary is below the initial level of the surface and there is a relatively large difference between the nominal and true contact area. The sink-in pattern is less evident at the nano-scale and the difference between the true and nominal contact area diminishes. As shown in Figure 14, the shape of the residual imprints for large and small tip radii in the scaled reference system z/h_{max}, x/R is not self-similar. The difference is also seen when the contact boundary is considered. At the nano-scale, it is close to circular while at the micro-scale it resembles a rounded square. It is interesting to note the vertical position of the contact boundary in the unloaded configuration for different tip radii (Figure 14). In all cases, the contact boundary lay below the level of the non-deformed surface. However, at the micro-scale it was formed deeper than at the nano-scale.

Qualitatively similar, but more distinct changes of the residual imprint topography with load in single crystal copper were reported also for indentation tests performed with a sharp Berkovich tip.[20] The contact boundary shifted up when the load decreased; it was formed below the initial level of the surface for high loads and above this level for low loads, and

consequently, the actual contact area did not change in self-similar manner when the load increased.

The specific evolution of residual impression with a change of the load and tip radius presented in this paper leads to the bilinear relationship $H^2 \sim \frac{1}{R}$ for the true hardness, that qualitatively agrees with $H^2 \sim \frac{1}{h}$ relationship proposed in the modified Nix–Gao model of the ISE for sharp indentation.[5–7]

The exhaustive physical explanation of the observed size effect characteristic requires TEM studies and is out of the scope of this paper. On the basis of the results presented in this paper, one can state that different deformation mechanisms are involved or different slip systems are activated in indentation tests performed at micro- and nano-scales when the same indentation strain (*i.e.,* h/R) is applied. This experimental result has not as yet been taken into account in simulations of ISE using strain gradient crystal plasticity models. In order to capture all aspects of the ISE, both the load-penetration curve and the topography of residual impression should be measured.

ACKNOWLEDGMENTS

This work has been supported by the National Science Centre (NCN) in Poland through Grant No. 2014/13/B/ST8/04286. The authors are very grateful to Dr Michal Maj for the SEM image of hardness impression morphology.

OPEN ACCESS

REFERENCES

1. T.T. Zhu, A.J. Bushby, and D.J. Dunstan: *Mater. Technol.*, 2008, vol. 23 (4), pp. 193–209.
2. W.D. Nix and H. Gao: *J. Mech. Phys. Solids*, 1998, vol. 46, pp. 411–25.
3. G. Feng and W.D. Nix: *Scr. Mater.*, 2004, vol. 51, pp. 599–603.
4. J.G. Swadener, E.P. George, and G.M. Pharr: *J. Mech. Phys. Solids*, 2002, vol. 50, pp. 681–94.
5. Y. Huang, F. Zhang, K.C. Hwang, W.D. Nix, G.M. Pharr, and G. Feng: *J. Mech. Phys. Solids*, 2006, vol. 54, pp. 1668–86.
6. K. Durst, B. Backes, and M. Goeken: *Scr. Mater.*, 2005, vol. 52, pp. 1093–97.
7. K. Durst, M. Goeken, and G.M. Pharr: *J. Phys.*, 2008, vol. 41, p. 074005.
8. M. Rester, C. Motz, and R. Pippan: *Acta Mater.*, 2007, vol. 55, pp. 6427–35.
9. M. Rester, C. Motz, and R. Pippan: *Phil. Mag. Lett.*, 2008, vol. 88, p. 879.
10. G.M. Pharr, E.G. Herbert, and Y. Gao: *Rev. Mater. Res.*, 2010, vol. 40, pp. 271–92.
11. Y.F. Gao, B.C. Larson, J.H. Lee, L. Nicola, J.Z. Tischler, and G.M. Pharr: *J. Appl. Mech.*, 2015, vol. 82, pp. 061007-1–061007-9.
12. C.S. Han, H. Gao, Y. Huang, and W.D. Nix: *J. Mech. Phys. Solids*, 2005, vol. 53, pp. 1188–1203.
13. H. Petryk and S. Stupkiewicz: *Arch. Mech.*, 2016, vol. 68 (6), pp. 459–85.
14. Y.Y. Lim and M.M. Chaudhri: *Philos. Mag.*, 1999, vol. A79, pp. 2979–3000.
15. I.J. Spary, A.J. Bushby, and N.M. Jennett: *Philos. Mag.*, 2006, vol. 86, pp. 33–35.
16. X.D. Hou, A.J. Bushby, and N.M. Jennett: *J. Phys. D Appl. Phys.*, 2008, vol. 41, p. 074006.
17. X.D. Hou and N.M. Jennett: *Acta Mater.*, 2012, vol. 60, pp. 4128–35.
18. L. Charleux, V. Keryvin, M. Nivard, J.P. Guin, J.C. Sangleboeuf, and Y. Yokoyama: *Acta Mater.*, 2014, vol. 70, pp. 249–58.
19. Y.H. Lee, J.H. Hahn, S.H. Nahm, J.I. Jang, and D. Kwon: *J. Phys. D Appl. Phys.*, 2008, vol. 41, p. 074027.
20. S. Kucharski and D. Jarzabek: *Metall. Mater. Trans. A*, 2014, vol. 45A, pp. 4997–5008.
21. A.J. Bushby and N. M. Jennett: *MRS Symp. Proc.*, 2001, 649 Q7.17.1.
22. A.C. Fisher-Crips: *Nanoindentation*, 2nd ed., Springer-Verlag, New York, 2004.
23. S. Shim, H. Bei, E.P. George, and G.M. Pharr: *Scr. Mater.*, 2008, vol. 59, pp. 1095–98.
24. S.K. Lawrence, D.F. Bahr, and H.M. Zbib: *J. Mater. Res.*, 2013, vol. 27 (24), pp. 3058–65.
25. P.S. Phani, K.E. Johanns, E.P. George, and G.M. Pharr: *J. Mater. Res.*, 2013, vol. 28 (19), pp. 2728–39.
26. S. Pathak, J.L. Riesterer, S.R. Kalidindi, and J. Michler: *Appl. Phys. Lett.*, 2014, vol. 105, pp. 161913-1–13-5.
27. J.S. Field and M.V. Swain: *J. Mater. Res.*, 1993, vol. 8 (2), pp. 207–306.
28. S. Biwa and B. Storakers: *J. Mech. Phys. Solids*, 1995, vol. 53, pp. 1303–33.
29. B. Eidel: *Acta Mater.*, 2011, vol. 59, pp. 1761–71.
30. R. Hill, B. Storakers, and A.B. Zdunek: *Proc. R. Soc. Lond.*, 1989, vol. 423, pp. 301–30.
31. H. Petryk, S. Stupkiewicz, and S. Kucharski: *Int. J. Solids Struct.*, 2017, vol. 112, pp. 209–21.
32. S.D.J. Mesarovic and N.A. Fleck: *Proc. R. Soc. Lond. A*, 1999, vol. 455, pp. 2707–28.
33. S. Stupkiewicz and H. Petryk: *Arch. Mech.*, 2016, vol. 68 (6), pp. 487–513.